A Wideband OAM Antenna Based on Chiral Harmonic Diffraction

Juan-Feng Zhu, Chao-Hai Du, *Senior Member, IEEE*, Wei E. I. Sha, *Senior Member, IEEE*, Zi-Wen Zhang, Zi-Chao Gao, Fan-Hong Li, and Pu-Kun Liu, *Senior Member, IEEE*

***Abstract*—An orbital angular momentum (OAM) antenna based on chiral harmonic diffraction of spoof surface plasmon polaritons (SSPP) is demonstrated in this letter. Due to the diffraction of the helical wire, SSPP is transformed into the high-purity OAM mode. The operation frequency is determined by SSPP, and the topological charge is manipulated by modulating the harmonic order. Additionally, this system achieves a frequency-controlled beam-scanning characteristic in a wide bandwidth from 7.8 to 12.6 GHz, and the measurement data agrees well with the theoretical analysis and the simulation results. Furthermore, the OAM antenna validated in this letter is compact, easy-fabricated, and robust. The underlying principle opens up a new train of thought for generating OAM mode and paves the versatile applications involving wireless communication.**

***Index Terms*—Helical wire, leaky-wave antenna, orbital angular momentum (OAM), spoof surface plasmon, vortex beam.**

I. Introduction

Orbital angular momentum (OAM) has drawn tremendous attention owing to its prospect for increasing communication capacity in recent years [1]–[4]. Being provided with unbounded eigenstates, OAM can offer multiple channels to enhance the transmission capacity without increasing the bandwidth in principle [5]. Hitherto, various approaches have been developed to generate electromagnetic waves carrying OAM mode [6]–[15]. The spiral phase plate is a widely used scheme because of its simple structure [6], [7]. The multiple OAM modes are generated in the metasurface structure, antenna array and ring resonators [7]-[15]. However, there are still some limitations. For example, the controlled phase-shift feeding network in the antenna array is essential but leads to an increase in cost and complexity. Moreover, the radiation direction be efficiently tuned, which is unfriendly and inconvenient for practical communication applications.

Manuscript received August 9, 2021; accepted August 22, 2021. Date of publication August 30, 2021; date of current version December 20, 2021. This work was supported in part by the National Natural Science Foundation of China under Grant 61861130367, Grant NSAF-U1830201, and Grant 61971013; in part by National Key Research in part by National Key Research and Development Program under Grant 2019YFA0210203; and in part by Newton Advanced Fellowship from Royal Society United Kingdom under Grant NAF/R1/180121. *(Corresponding author: Chao-Hai Du.)*

Juan-Feng Zhu, Chao-Hai Du, Zi-Wen Zhang, Zi-Chao Gao, Fan-Hong Li, and Pu-Kun Liu are with the State Key Laboratory of Advanced Optical Communication Systems and Networks, Department of Electronics, Peking University, Beijing 100871, China (e-mail: zhujuanfeng@pku.edu.cn; duchaohai@pku.edu.cn; zhangziwen@pku.edu.cn; gaozc@pku.edu.cn; fanhonglee@pku.edu.cn; pkliu@pku.edu.cn).

Wei E. I. Sha is with the Key Laboratory of Micro-nano Electronic Devices and Smart Systems of Zhejiang Province, College of Information Science and Electronic Engineering, Zhejiang University, Hangzhou 310027, China (e-mail: weisha@zju.edu.cn).

Digital Object Identifier 10.1109/LAWP.2021.3108553

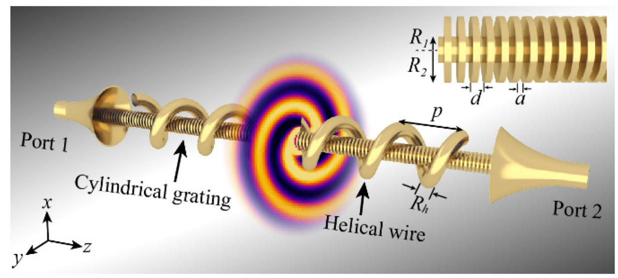

Fig. 1. Schematic diagram of the OAM antenna. Inset: the cylindrical grating.

The development of the spoof surface plasmon polaritons (SSPP) provide a alternative way for generating OAM mode. SSPP imitates the optical surface plasmon polaritons in the microwave and the terahertz range, which is further tuned by constructing structural parameters [16]. SSPP has been widely applied to various fields and is utilized to generate the OAM modes [17]-[20]. Localized SSPP in a flat spiral structure is utilized to produce OAM modes with specific topological charges (TCs, l) [21], [22]. Besides, SSPP-carried OAM modes can be excited in a helical grating, indicating that the helical structure can efficiently modulate the azimuthal phase and generate the OAM mode consequently [23].

In this letter, a wideband harmonic-controlled OAM antenna based on SSPP is demonstrated. The SSPP is converted into the OAM mode by the diffraction of a helical wire. The TC of the OAM mode is related to the diffraction harmonic orders and the chirality of the helical wire. The radiation direction is tailored by the operating frequency, leading to a broadband beam-scanning characteristic. Furthermore, the system shows strong robustness in fabrication and assembling. The demonstrated OAM antenna not only expands the application of SSPP but also facilitates its applications in the communication system.

II. Design and Verification of Antenna

A. Generating OAM via the Diffraction of Helical Wire

The OAM antenna, including an cylindrical grating and a helical wire, is illustrated in Fig. 1. The SSPP wave propagates along the cylindrical grating and is transformed into the OAM mode via the helical wire. This design is an extended version of our previous work [24]. In [24], the SSPP is excited by a free-electron bunch and converted into the OAM beam radiation via the helical wire. However, there are several experimental challenging factors. For example, a complex system for generating, focusing, and collecting electron beam is required. Compared with [24], the OAM antenna is much convenient and feasible. To explore the physical mechanism, the characteristic of SSPP on a cylindrical grating is introduced first.

Since SSPP decays exponentially perpendicular to the direction of propagation, the electric field is expressed as [25]

$$E\ (r, \varphi, z) = \sum_{m=-\infty}^{\infty} F_{vm}\ (r)\ e^{jm\varphi} e^{-jk_{zm} z} \tag{1}$$

where A_n is the coefficient of the n-th SSPP harmonic order. k_{zn} is the longitudinal wavenumber, $k_{zn} = k_{z0}\ + 2\pi n/d$. k_{rn} is the radial wavenumber, and $k_{zn}^2 -\ k_{rn}^2 = k_0^2$. K_0 is the modified zeroth Bessel function of the second. The working frequency is obtained via the dispersion relation. The dispersion equation is given based on the PEC model as follows [26]:

$$\sum_{n\ =\ -\infty}^{\infty} S_n^2 \frac{k_0}{k_{rn}} \frac{K_1\ (k_{rn} r_2)}{K_0\ (k_{rn} r_2)} \times \frac{N_0\ (k_0 r_2)\ J_0\ (k_0 r_1) - N_0\ (k_0 r_1)\ J_0\ (k_0 r_2)}{N_0\ (k_0 r_1)\ J_1\ (k_0 r_2) - N_1\ (k_0 r_2)\ J_0\ (k_0 r_1)} = 1 \tag{2}$$

where $S_n = \sqrt{a/d}\ \mathrm{sinc}(k_{zn} a/2)$. J_i and N_i are the i-th Bessel and Neumann functions, respectively.

According to Floquet's theorem, the electric field in helical wire presents the following properties [25].

(i) The field remains invariant with moving a distance *mp* in the z-direction, where *m* is an integer.

$$E\ (r, \varphi, z)\ =\ F\ (r, \varphi, z)\ e^{-j\beta_0 z} \tag{3a}$$

$$F\ (r, \varphi, z + mp)\ =\ F\ (r, \varphi, z) \tag{3b}$$

where $F(z)$ is a periodic function about z.

(ii) The field also remains unchanged when the helical wire rotates 2π around the z-axis.

$$F\ (r, \varphi + 2\pi, z) =\ F\ (r, \varphi, z)\ . \tag{4}$$

In satisfying the two conditions above, the function $F(r, \varphi, z)$ must be of the following form:

$$F\ (r, \varphi, z) = \sum_{v=-\infty}^{\infty} \sum_{m=-\infty}^{\infty} F_{vm}\ (r)\ e^{jv\varphi}\ e^{-j2\pi mz/p}. \tag{5}$$

(iii) When the grating is moved by an distance δz and rotated in φ by $\delta\varphi = 2\pi\delta z/p$, the EM wave remains invariant. This gives

$$F\ (r, \varphi + 2\pi\delta z/p, z + \delta z) =\ F\ (r, \varphi, z)\ . \tag{6}$$

It yields

$$\sum_{v\ =\ \infty}^{\infty} \sum_{m\ =\ -\infty}^{\infty} F_{vm} e^{jv(\varphi + 2\pi\delta z/p)} e^{-j2\pi m(z+\delta z)/p} = \sum_{v=\infty}^{\infty} \sum_{m=-\infty}^{\infty} F_{vm} e^{jv\varphi} e^{-j2\pi mz/p}. \tag{7}$$

To ensure this, it is necessary to demand $v = m$, i.e.,

TABLE I

PARAMETERS FOR THE OAM ANTENNA

Parameter	Value	Description
R_1	2 mm	Inner radius
R_2	6 mm	Outer radius
a	1 mm	Width of cylindrical grating
d	2 mm	Period of cylindrical grating
g	1.5 mm	Gap between grating and helical wire
p	8d	Period of the helical wire
R_h	4.5 mm	Radius of the helical wire

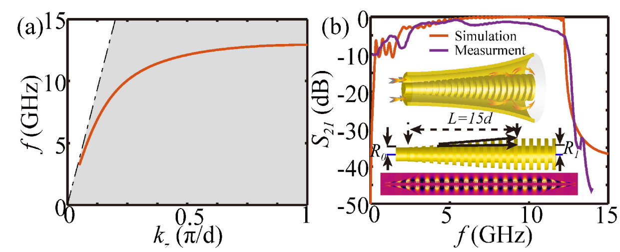

Fig. 2. (a) Dispersion curve of the cylindrical grating. (b) Transmission characteristic of the waveguide–SSPP coupler. Top inset: Schematic model of the coupler. Bottom inset: Electric field distribution at 10 GHz.

$F_{vm}(r) \neq 0$, for $v = m$, and $F_{vm}\ (r) =\ 0$, for $v \neq m$ so, $F(r, \varphi, z)$ must be in the following expanded series:

$$F\ (r, \varphi, z) = \sum_{m=-\infty}^{\infty} F_m\ (r)\ e^{jm\varphi} e^{-j2\pi mz/p}. \tag{8}$$

The field components must be the form

$$E\ (r, \varphi, z) = \sum_{m=-\infty}^{\infty} F_m\ (r)\ e^{jm\varphi} e^{-j\beta_{zm} z} \tag{9}$$

where $\beta_{zm} = \beta_0\ + 2\pi m/p$ is the wavenumber of the m-th harmonic order. $k_0 =\ \omega/c$ is the wavenumber. The phase component $e^{jm\varphi}$ indicates that the EM wave carries the OAM mode in the helical wire, and the TC is given by

$$l\ =\ \pm |m| \tag{10}$$

where $\pm$ represents the rotation direction of OAM mode and is determined by that of the helical wire.

With the diffraction the longitudinal wavenumber of SSPP is modified as (11) with adding the diffraction wavenumber

$$k_z = k_{zn}\ + 2m\pi/p \tag{11}$$

where m is the diffraction order. If $|k_z| < k_0$, SSPP is radiated into free space. The radiation angle can be derived based on the principle of the leaking-wave antenna [27]

$$\theta\ =\ \mathrm{acos}\,(k_z/k_0)\ . \tag{12}$$

In brief, the helical grating plays two roles in the generation of the OAM mode. First, it provides the wavenumber compensation for converting SSPP into a radiated beam. Second, it modulates the azimuthal phase distribution to generate the OAM mode.

B. Design of the SSPPs Coupler

The optimized parameters are listed in Table I, and the dispersion curve is shown in Fig. 2(a). As $k_{zn} > k_0$, SSPP is confined to the surface of the grating. Due to the mismatch between k_{zn} and k_0, SSPP cannot be excited directly. In this

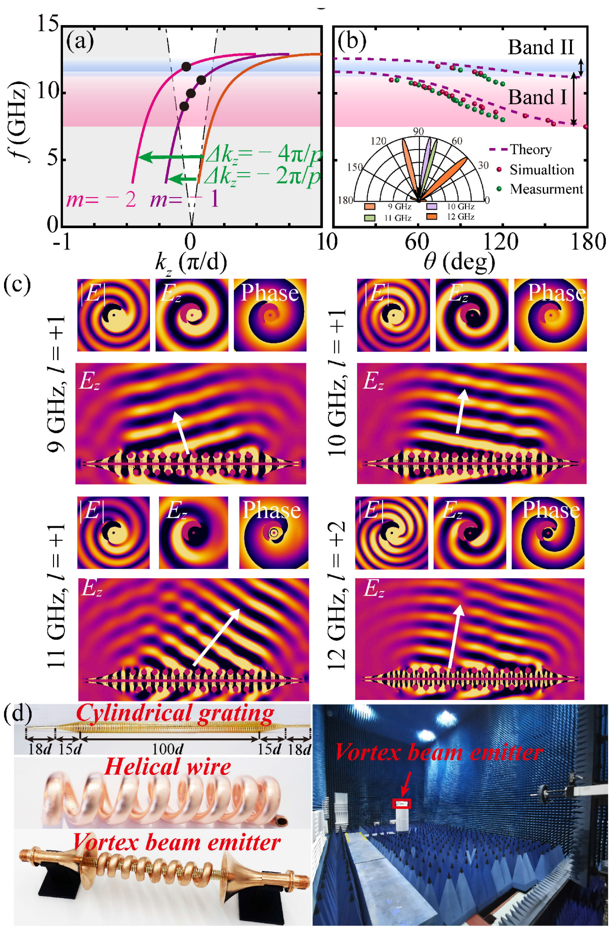

Fig. 3. Simulation and experimental results of the OAM antenna. (a) Brillouin diagram with $p = 8d$. (b) Radiation angle versus the operating frequency. Inset: Radiation pattern at different frequencies. (c) Electric field distributions with different TCs. (d) Left: Fabricated cylindrical grating, the helical wire, and the OAM antenna. Right: Experimental setup of the OAM antenna.

way, a coupler is specially designed and is presented in the inset of Fig. 2(b). The coupler, which is composed of a gradient grating and a horn, can achieve efficient conversion between the waveguide mode and the SSPP mode [28]. The inner radius is $R_0 = 1.52$ mm and is the same as that of the coaxial connector. The inner and outer radii gradually increase from R_0 to R_1 and R_2, respectively. The optimized length of the gradient section is $L = 15d$. The profile of the horn is described as $y = C_1 e^{\alpha x} + C_2$, where $C_1 = (y_2 - y_1)/(e^{\alpha x_2} - e^{\alpha x_1})$, $C_2 = (y_2 e^{\alpha x_2} - y_1 e^{\alpha x_1})/(e^{\alpha x_2} - e^{\alpha x_1})$, and $\alpha = 0.02$. The start and end points are set as $(x_1, y_1) = (0, 0)$ and $(x_2, y_2) = (20d,\ 5R_2)$, respectively. To verify the transmission properties, a pair of couplers is set at both ends of the cylindrical grating to smoothly bridge SSPP and coaxial mode. The working performance can be verified by CST Studio [29]. The transmission property is presented as the red line in Fig. 2(b). The transmission bandwidth is about 9.5 GHz from 3 to 12.5 GHz, and the maximum coupling efficiency is about 99%. The fabricated grating and coupler are shown in Fig. 3(d), and the experimental result is shown as the purple line. As the wavelength in the low-frequency range (0–3 GHz) is longer than that of the high-frequency range (3–12.5 GHz), the electromagnetic wave in the low-frequency range cannot be efficiently suppressed by the coupler. It means that a part of the energy fails to be converted into SSPP and escapes from the coupler. Consequently, the leaked energy results in a low transmission rate.

C. Generation of the OAM Beam

As (11) indicates, the dispersion curve will shift along k_z axis because of the diffraction effect, and the deviation distance is $\Delta\ k_z = 2\pi m/p$. If the dispersion curve is shifted into the fast-wave region, SSPP can be transformed into the spatial OAM beam. The shifted dispersion curves are shown in Fig. 3(a). The working frequency range is obtained via the intersection points of dispersion curves and light cone. Two working ranges corresponding to -1st and -2nd harmonic orders are marked as pink and blue zones in Fig. 3(b). The bands I and II are 7.8–11.6 GHz and 11.2–12.6 GHz, respectively. As (8) indicates, TCs are $l = +1$ and $l = +2$ in bands I and II, respectively. The electric field distributions at 9, 10, 11, and 12 GHz are presented in Fig. 3(c), and TCs are $l = +1$, $l = +1$, $l = +1$, and $l = +2$, respectively. The TC distributions agree well with the theoretical analysis. It is worth pointing that the propagation direction of the vortex beam has an angle with the z-axis. As it is difficult to observe the radiation pattern on a conical surface, the transversal observation plane is presented in the xy-plane. As the cylindrical grating is located at the center, the phase singularity is absent.

Similar to a leaky antenna, this system can achieve a frequency-controlled beam-scanning characteristic in each band. The radiation direction can be approximatively acquired from (12) and is shown as the dashed line in Fig. 3(b). Inset of Fig. 3(b) shows the radiation pattern at 9–12 GHz, and the radiation angles are 107°, 85°, 42°, and 76°, respectively. The beam-scanning characteristic is also proved by the experiment. The fabricated antenna and experimental scene are shown in Fig. 3(d). A port of the antenna is connected to the vector network analyzer, and the other port is connected to a matching load to reduce the reflection. The measured radiation angle is in accordance with the simulation analysis. The helical wire is blocked up by a piece of foam to be coaxial with the cylindrical grating in the experiment. Unavoidably impacted by the helical wire, the dispersion curve of SSPP is slightly changed. The simulation results deviate slightly from the theoretical prediction consequently. For the difference between the simulation and experimental results, the explanations are presented as follows. First, the manufacturing errors inevitably affect the radiation performance. Second, the cylindrical grating and helical wire cannot be perfectly coaxial and can be avoided by optimizing structural parameters and improving the assembling precision. As limited by the experimental conditions, the phase and electric distributions cannot be observed directly, whereas the beam-scanning and the OAM characteristics are related to each other. In other words, the OAM characteristics can be proved indirectly by the verification of the beam-scanning function.

The gain and efficiency are illustrated in Fig. 4(a). The average gain is near 10 dB, and the maximum is 12 dB at 10.5 GHz. The average efficiency is about 50%, and the maximum is about 80%. The far-field radiation pattern at 10 GHz is plotted in Fig. 4(b).

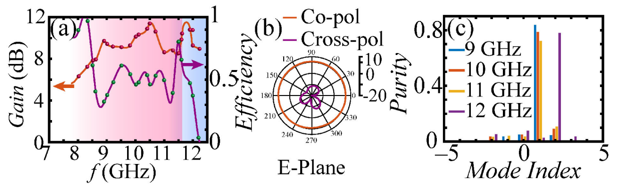

Fig. 4. (a) Gain and efficiency of the OAM antenna. (b) Radiation pattern of the copolarization and cross polarization in the *E*-plane at 10 GHz. (c) Normalized mode purities of the OAM mode at various frequencies.

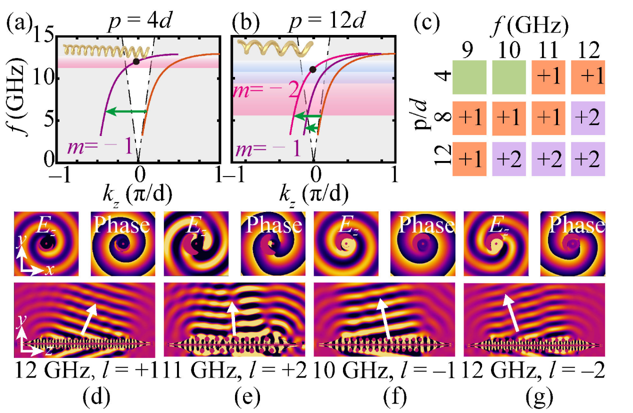

Fig. 5. (a) and (b) Brillouin diagrams with $p = 4d$ and $p = 12d$. (c) Distribution map of TCs. (d) and (e) Electric field distributions with $p = 4d$ and $p = 12d$. (f) and (g) Electric field distributions with reversing the helical wire's chirality.

The gain of the copolarization and cross polarization is 10.5 dB and −11 dB, respectively, which implies that the OAM emitter is linear polarization with a low cross-polarization level. The purity is a significant index to evaluate the performance of the OAM mode, and the normalized results are shown in Fig. 4(c). Based on the principle of Fourier transform, the purity of each mode can be obtained as follows:

$$p\ [l] = \frac{1}{2\pi} \int_0^{2\pi} \psi\left(\varphi\right) d\varphi \mathrm{e}^{(-jl\varphi)} \tag{13}$$

where l is the topological charge, ψ is the phase distribution, and φ represents the azimuthal angle. The data are discrete in practical processing. Then, (13) is modified as follows:

$$p\ [l] = \frac{1}{N} \sum_{n=1}^{N} \psi\left(\varphi_n\right) \mathrm{e}^{(-jl\varphi_n)} \tag{14}$$

where N is the number of sampling points. These calculated data points are extracted from a circle with $R = 25$ mm. The maximum and minimum purities are 0.84 and 0.78 at 9 GHz and 11 GHz, respectively.

Inspired by (8)–(12), the TC is manipulated by the diffraction order, which can be realized by tuning p. When $p = 8d$ is changed into $p = 4d$, the dispersion curve with phase shift under −1st harmonic diffraction is shown in Fig. 5(a). SSPP is converted into a spatial OAM beam with TC $l = +1$ at 12 GHz. Similarly, TC is changed as $l = +2$ at 11 GHz with $p = 12d$. The distribution map of TCs with different pitches is shown in Fig. 5(c). Furthermore, the helical wire can be replaced by a metal spring. When the metal spring is connected to a mechanical motor, the variation of the period can be automatically modulated. In this way, a mechanical tunable OAM antenna is effectively achieved.

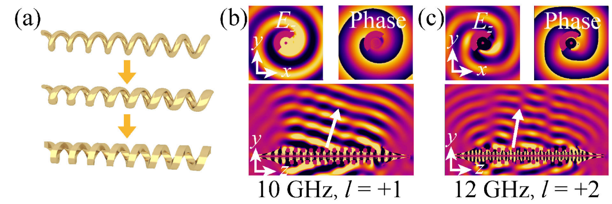

Fig. 6. (a) Deformation of the helical wire. (b) and (c) Electric distributions of the OAM mode with the deformed helical grating.

Besides, there are two approaches to tune the sign of TC. First, the chirality of the OAM mode is reversed by changing the feed port, as shown in Fig. 5(f) and (g). Second, altering the chirality of the helical wire. To sum up, the system shows significant flexibility in the manipulation of TC, including the mode index and the rotation direction.

This system is superior to the OAM beam generated by the conventional resonant structures in respect to robustness to the fabrication and assembling errors [15], [21], [22]. To evaluate the influence of deformation induced by the fabrication errors, the fabrication tolerance of helical wires is discussed. If the helical wire becomes deformed, the transversal form is changed from a circular into a rectangular, as shown in Fig. 6(a), and the OAM mode can also be generated. As the structural parameters of the grating remain unchanged, the operating frequency remains constant as a result. The OAM modes with TCs $l = +1$ and $l = +2$ are generated at 10 and 12 GHz, as shown in Fig. 6(b) and (c), respectively. In other words, as long as SSPP is diffracted into the free space via the helical wire, the OAM mode can be excited. Furthermore, the introduced method can be applied not only in the microwave region but also in the millimeter–terahertz region.

Due to the prominent properties of the OAM antennas, the OAM antenna is promising for wideband communication systems. First, it is likely to realize a point-to-point communication with appropriate parameters based on the beam-scanning function. Second, the radiation pattern can also be converted into directional radiation by a parabolic surface, and the divergence angle is reduced consequently. Third, the OAM antenna may also achieve a fast switch of channels and enhance the capacity of the communication system based on the tunability of the TC. Finally, TC is fixed at each operating band. It can be utilized to achieve wideband communication.

III. Conclusion

In summary, a wideband OAM antenna is demonstrated in this letter. The OAM mode is generated from SSPP via the diffraction of the helical wire. By switching the harmonic order, this system can work in different frequency ranges. Beam-scanning characteristic is observed and experimentally verified in each range. The TC can be flexibly tuned by the variation of the harmonic order and the chirality. The mode purity of the OAM mode exceeds 0.8, and the average gain is 10 dB. Moreover, this system has strong robustness and can work in a wide frequency band. The antenna provides a simple but efficient way to achieve an OAM beam. It is anticipated that the antenna will promote applications in communication systems.

Acknowledgment

The authors would like to thank Dr. B.-L. Hao from Beijing Vacuum Electronics Research Institute, China, for his support for CST software and professional suggestions in the letter.

References

[1] D. Lee, H. Sasaki, H. Fukumoto, K. Hiraga, and T. Nakagawa, "Orbital angular momentum (OAM) multiplexing: An enabler of a new era of wireless communications," *IEICE Trans. Commun.*, vol. 100, no. 7, pp. 1044–1063, Jul. 2017.

[2] G. Gibson *et al.*, "Free-space information transfer using light beams carrying orbital angular momentum," *Opt. Exp.*, vol. 12, no. 22, pp. 5448–5456, Nov. 2004.

[3] X. Hui *et al.*, "Multiplexed millimeter wave communication with dual orbital angular momentum (OAM) mode antennas," *Sci. Rep.*, vol. 5, May 2015, Art. no. 10148.

[4] O. Edfors and A. J. Johansson, "Is orbital angular momentum (OAM) based radio communication an unexploited area?," *IEEE Trans. Antennas Propag.*, vol. 60, no. 2, pp. 1126–1131, Feb. 2012.

[5] P. Miao *et al.*, "Orbital angular momentum microlaser," *Science*, vol. 353, no. 6298, pp. 464–467, Jul. 2016.

[6] M. W. Beijersbergen, R. P. C. Coerwinkel, M. Kristensen, and J. P. Woerdman, "Helical-wavefront laser beams produced with a spiral phaseplate," *Opt. Commun.*, vol. 112, no. 5/6, pp. 321–327, Dec. 1994.

[7] E. Brasselet, M. Malinauskas, A. Zukauskas, and S. Juodkazis, "Photopolymerized microscopic vortex beam generators: Precise delivery of optical orbital angular momentum," *Appl. Phys. Lett.*, vol. 97, no. 21, Nov. 2010, Art. no. 211108.

[8] R. C. Devlin, A. Ambrosio, N. A. Rubin, J. P. Balthasar Mueller, and F. Capasso, "Arbitrary spin-to–orbital angular momentum conversion of light," *Science*, vol. 358, no. 6365, pp. 896–901, Nov. 2017.

[9] H. Shi *et al.*, "Generation of multiple modes microwave vortex beams using active metasurface," *IEEE Antennas Wireless Propag. Lett.*, vol. 18, no. 1, pp. 59–63, Jan. 2019.

[10] N. Kou, S. Yu, and L. Li, "Generation of high-order Bessel vortex beam carrying orbital angular momentum using multilayer amplitude-phase-modulated surfaces in radiofrequency domain," *Appl. Phys. Exp.*, vol. 10, Dec. 2016, Art. no. 016701.

[11] Y. Yang, K. Guo, F. Shen, Y. Gong, and Z. Guo, "Generating multiple OAM based on a nested dual-arm spiral antenna," *IEEE Access*, vol. 7, pp. 138541–138547, 2019.

[12] W. Zhang *et al.*, "Four-OAM-mode antenna with traveling-wave ring-slot structure," *IEEE Antennas Wireless Propag. Lett.*, vol. 16, pp. 194–197, 2017.

[13] A. Tennant and B. Allen, "Generation of OAM radio waves using circular time-switched array antenna," *Electron. Lett.*, vol. 48, no. 21, pp. 1365–1366, 2012.

[14] S. Zheng, X. Hui, X. Jin, H. Chi, and X. Zhang, "Transmission characteristics of a twisted radio wave based on circular traveling-wave antenna," *IEEE Trans. Antennas Propag.*, vol. 63, no. 4, pp. 1530–1536, Apr. 2015.

[15] J. Xu *et al.*, "Generation of continuously variable-mode orbital angular momentum beams," *Eng. Sci.*, vol. 10, pp. 51–57, Dec. 2020.

[16] J. B. Pendry, L. Martin-Moreno, and F. J. Garcia-Vidal, "Mimicking surface plasmons with structured surfaces," *Science*, vol. 305, no. 5685, pp. 847–849, Aug. 2004.

[17] T.-J. Huang, L.-Z. Yin, Y. Shuang, J.-Y. Liu, Y. Tan, and P.-K. Liu, "Far-field subwavelength resolution imaging by spatial spectrum sampling," *Phys. Rev. Appl.*, vol. 12, no. 3, Sep. 2019, Art. no. 034046.

[18] T.-J. Huang, H.-H. Tang, Y. Tan, L. Li, and P.-K. Liu, "Terahertz super-resolution imaging based on subwavelength metallic grating," *IEEE Trans. Antennas Propag.*, vol. 67, no. 5, pp. 3358–3365, May 2019.

[19] J. Y. Yin, J. Ren, L. Zhang, H. Li, and T. J. Cui, "Microwave vortex-beam emitter based on spoof surface plasmon polaritons," *Laser Photon. Rev.,* vol. 12, no. 3, Mar. 2018, Art. no. 1870020.

[20] Z. Liao *et al.*, "Microwave-vortex-beam generation based on spoof-plasmon ring resonators," *Phys. Rev. Appl.*, vol. 13, no. 5, May 2020, Art. no. 054013.

[21] L. Yuan *et al.*, "Localized plasmonic vortex printing technology based on the metaparticle and spoof surface plasmon polaritons," *Phys. Status Solidi A*, vol. 218, no. 8, Feb. 2021, Art. no. 2000708.

[22] Y. Zhang, Q. Zhang, C. H. Chan, E. Li, J. Jin, and H. Wang, "Emission of orbital angular momentum based on spoof localized surface plasmons," *Opt. Lett.*, vol. 44, no. 23, pp. 5735–5738, Dec. 2019.

[23] F. Rüting, A. I. Fernandez-Dominguez, L. Martin-Moreno, and F. J. Garcia-Vidal, "Subwavelength chiral surface plasmons that carry tuneable orbital angular momentum," *Phys. Rev. B*, vol. 86, no. 7, Aug. 2012, Art. no. 075437.

[24] J.-F. Zhu *et al.*, "Free-electron-driven orbital angular momentum emitter," presented at the 13th UK-Eur.-China Workshop Millimetre-Waves Terahertz Technol., 2020. [Online]. Available: https://ieeexplore.ieee.org/abstract/document/9296116

[25] K. Zhang and D. Li, *Electromagnetic Theory for Microwaves and Optoelectronics*. New York, NY, USA: Springer, 2008.

[26] S. A. Maier, S. R. Andrews, L. Martin-Moreno, and F. J. Garcia-Vidal, "Terahertz surface plasmon-polariton propagation and focusing on periodically corrugated metal wires," *Phys. Rev. Lett.*, vol. 97, no. 17, Oct. 2006, Art. no. 176805.

[27] J.-F. Zhu, C.-H. Du, T.-J. Huang, L.-Y. Bao, S. Pan, and P.-K. Liu, "Free-electron-driven beam-scanning terahertz radiation," *Opt. Exp.*, vol. 27, no. 18, pp. 26192–26202, Aug. 2019.

[28] H.-H. Tang, T.-J. Ma, and P.-K. Liu, "Experimental demonstration of ultra-wideband and high-efficiency terahertz spoof surface plasmon polaritons coupler," *Appl. Phys. Lett.*, vol. 108, no. 19, May 2016, Art. no. 191903.

[29] CST Studios, CST Microwave Studio, 2008. [Online]. Available: https://www.3ds.com/products-services/simulia/products/cst-studio-suite/